PAPER • OPEN ACCESS

Core plasma fueling by fast inward particle transport after hydrogen pellet injection in Wendelstein 7-X

To cite this article: H. Damm *et al* 2026 *Nucl. Fusion* **66** 026031

OPEN ACCESS
IOP Publishing | International Atomic Energy Agency
Nuclear Fusion
Nucl. Fusion **66** (2026) 026031 (18pp)
https://doi.org/10.1088/1741-4326/ae2a4f

Core plasma fueling by fast inward particle transport after hydrogen pellet injection in Wendelstein 7-X

H. Damm[1,*], J. Baldzuhn[1], R.C. Wolf[1], T.S. Petersen[1], J. Schilling[1], N. Panadero[2], S.A. Bozhenkov[1], C. Brandt[1], K.J. Brunner[1], G. Fuchert[1], J. Knauer[1], A. Langenberg[1], S. Kwak[1], N.A. Pablant[3], E. Pasch[1], H. Thomsen[1] and the W7-X Team[a]

[1] Max-Planck-Institut für Plasmaphysik, D-17491 Greifswald, Germany
[2] Laboratorio Nacional de Fusión, CIEMAT, 28040 Madrid, Spain
[3] Princeton Plasma Physics Laboratory, Princeton University, Princeton, NJ 08543, United States of America

E-mail: hannes.damm@ipp.mpg.de

Received 23 May 2025, revised 27 October 2025
Accepted for publication 9 December 2025
Published 13 January 2026

Abstract

A large database of more than 1000 individual cryogenic hydrogen pellets injected into Wendelstein 7-X for plasma fueling was analyzed to improve the understanding of the three phases of the process: the ablation, deposition and transport of the pellet material. Kilohertz-sampled electron density and temperature measurements revealed a more complex drift behavior than predicted by numerical code simulation. It could be explained by the poloidal plasma $\boldsymbol{E}_\mathrm{r} \times \boldsymbol{B}$ - drift rotation, which plays a significant role in stellarators, but was not previously considered in pellet injection codes like HPI2. The drift results in a fast poloidal rotation of the pellet material around the plasma core, leading to an almost homogeneous deposition over the involved flux surfaces regardless of magnetic high and low field side injection geometry. Additionally, a novel fast inward directed transport mechanism ('FIT-effect') was observed. The effect occurs on timescales of tens of milliseconds and cannot be explained by neoclassical transport or diffusion. It might be linked to the turbulence pinch recently found in Wendelstein 7-X. When the FIT-effect occurs, the pellet particles are rapidly transferred from the deposition flux surfaces to the plasma core, causing the plasma density profile to peak, which is beneficial for confinement in Wendelstein 7-X. The large pellet injection database was statistical analyzed with regard to pellet and plasma parameters, which delivered some starting points towards developing an understanding of the physics behind the FIT-effect. The results indicate, that plasma core fueling via pellet injection is largely independent of the injection geometry in stellarators under certain conditions, reducing the technical complexity of the injection system.

[a] See Grulke *et al* 2024 (https://doi.org/10.1088/1741-4326/ad2f4d) for the W7-X Team.
[*] Author to whom any correspondence should be addressed.

Supplementary material for this article is available online

Keywords: pellet injection, central particle fueling, particle transport, heat transport, Wendelstein 7-X

1. Introduction

Cryogenic pellet injection [1] is an established means for deep and efficient particle fueling in magnetically confined [2] fusion plasmas [3–6]. After the first phase of ablation [7], i.e. the sublimation of ice particles to neutral dense clouds within about $t_{\mathrm{ablation}} \sim \mathcal{O}(1\,\mathrm{ms})$, the pellet particles are ionized and form the so-called plasmoids [8], which expand parallel to the field lines, as most simplified approximation. In toroidal magnetic configurations [9–11], the plasmoids are polarized by the charged particle separation as a consequence of the $\nabla \boldsymbol{B}$ - drift [12] induced by the toroidal curvature of the plasma. This results in a vertical electric field $\boldsymbol{E}_{\nabla \mathrm{B}}$ within the plasmoids. This electric field leads to a subsequent plasmoid drift, which is to lowest order an $\boldsymbol{E}_{\nabla \mathrm{B}} \times \boldsymbol{B}$ - drift to the magnetic low field side direction (LFS) [12]. As exploited in tokamaks [10, 11], the $\boldsymbol{E}_{\nabla \mathrm{B}} \times \boldsymbol{B}$ - drift can be used for the optimization of deep core fueling by magnetic high field side (HFS) injection [4]. In addition, the $\boldsymbol{E}_{\mathrm{r}} \times \boldsymbol{B}$ - drift of the background plasma affects the final deposition location of the pellet particles as well. The ambipolar radial electric field $\boldsymbol{E}_{\mathrm{r}}$ is a fundamental plasma parameter in a stellarator plasma [13]. It results from the intrinsically non-ambipolar radial particle fluxes, i.e. from the different amounts of the radial electron and ion fluxes, which build up an electrostatic potential within the plasma. Each flux surface has a constant potential. It is found that anomalous particle fluxes are intrinsically ambipolar, and contribute therefore not to the formation of $\boldsymbol{E}_{\mathrm{r}}$. To fulfill the force balance equation, a balancing $\boldsymbol{E}_{\mathrm{r}} \times \boldsymbol{B}$ plasma drift rotation occurs, which is charge independent; in contrast to the diamagnetic drift rotation. The $\boldsymbol{E}_{\mathrm{r}} \times \boldsymbol{B}$ - drift in stellarators has a toroidal and a poloidal component, where the poloidal component dominates over the toroidal because of the missing axis-symmetry, as opposed to the more toroidal rotation in axisymmetric tokamaks [14]. Hence, the formation of $\boldsymbol{E}_{\mathrm{r}}$ results from the magnitude of the radial particle fluxes. On the other hand, the magnitude of the neoclassical transport coefficients (and therefore the amount of the radial particle fluxes) strongly depend on the value of $\boldsymbol{E}_{\mathrm{r}}$. The size of $\boldsymbol{E}_{\mathrm{r}}$ and the ion temperature (T_{i}) can be determined numerically by neoclassical transport calculations and the solution of the ambipolarity constraint [15]. Experimentally, the spatially resolved spectroscopic measurement of Doppler shifted impurity line radiation profiles determined via an x-ray Imaging Crystal Spectrometer (XICS) [16] provides the size of the $\boldsymbol{E}_{\mathrm{r}} \times \boldsymbol{B}$ plasma drift, and hence the $\boldsymbol{E}_{\mathrm{r}}$ radial profile [17]. The time scale of the so called 'deposition' phase - within the drifts occur - is of $\sim \mathcal{O}(10\,\mathrm{ms})$ under the typical plasma conditions in our experiments. The timescale of the plasma particle transport is typically about one order of magnitude larger. In this work we present pellet experiments performed at Wendelstein 7-X (W7-X) [18] during the OP1.2b experimental campaign. In an earlier analysis of these experiments [6], we found a much higher fueling efficiency for LFS-injected pellets (experiment 70% vs. prediction 50%) and a lower fueling efficiency for HFS-injected pellets (experiment 88% vs. prediction up to 98%) than expected. Accordingly, the difference between HFS and LFS injection fueling efficiencies was much weaker: prediction 100% vs. experiment 26%. We expected that the magnetic field properties, for example the smaller $\nabla \boldsymbol{B}$, as compared to a tokamak, altered the ablation and deposition process and hence the fueling. To test this hypothesis, we reviewed the pellet injection process with a focus on the fast density and temperature perturbations pellets introduce to the plasma as well as on the subsequent particle drift and transport. We used fast sampled Thomson scattering (TS) 'Burst-Mode' profiles [19] to resolve pellet effects in the plasma electron temperature and density on timescales down to 0.1 ms as well as 30 Hz 'Standard-Mode' TS profiles. They were, together with x-ray tomographic reconstruction methods [20], employed to investigate the time phase of particle deposition and subsequent fast transport.

In this paper, the different phases of the pellet injection will also be analyzed statistically, based on experimental data gained from about 1000 individual pellets injected to the stellarator W7-X.

In section 2, the W7-X experiment, the pellet injector and the most important diagnostics delivering data for this study, namely the TS diagnostic [21] and the x-ray multi-camera tomography system (XMCTS) [22] will be briefly described. The parameters included in the statistical analysis are introduced as well. The central mathematical description of the employed statistical method can be found in A. The first part (3.1) of the results in section 3 starts with a consideration of the pellet ice ablation as an initial step, delivering the starting distribution of the neutral pellet particles. In the second part (3.2), the observation of the cloud and plasma drift phenomena after ionization of the neutrals into cold and dense plasmoids will be presented. We show the 'FIT-effect', a **f**ast **i**nward **t**ransport of particles across the magnetic field surfaces, in the third part (3.3) of the results. Finally possible actuators for the FIT-effect are examined and analyzed regarding their statistical significance using the large pellet injection database in section 4.

The observations are discussed in section 5 with a focus on the implications for the improvement of pellet injection theory

and numerical code development as well as the design of future core fueling pellet injectors and the development of adequate core-fueling and plasma scenarios.

2. Experiment

2.1. Hardware setup

W7-X is a fivefold symmetric toroidal plasma experiment [18, 23]. Its 70 superconducting coils produce a steady-state magnetic field to contain a plasma of about $\langle r_{\mathrm{LCFS}} \rangle = 0.5\,\mathrm{m}$ minor radius and $\langle R_{\mathrm{Axis}} \rangle = 5.5\,\mathrm{m}$ major radius. By varying the individual coil currents, different magnetic configurations are possible changing e.g. the rotational transform ι - the number of poloidal transits of a field line on a toroidal flux surface in one toroidal turn. The most pellet experiments were performed employing the 'standard' configuration with $\iota(\langle r_{\mathrm{LCFS}} \rangle) \approx 5/5$ although we did not restrict ourselves to this configuration.

The 'blower-gun' type W7-X pellet injector [24] generates cylindrical ($d = 2\,\mathrm{mm}$, $l = 2\,\mathrm{mm}$) solid H_2 ice pellets, which are transferred alternately to the HFS and LFS ports via steel guiding tubes of 29 m and 15 m length, respectively. The designed flight paths inside the plasma at a toroidal angle of $\Phi = 232.0^\circ$ are indicated in red for HFS pellets and blue for LFS pellets in figure 1(*a*). The distance of free flight from the end of the tube to the plasma edge measures 2.3 m for both sides. The injection frequency could be set to 15…30 Hz. The pellet velocity typically varied between $160\ldots210\,\mathrm{m\,s^{-1}}$ and the pellets arriving at the plasma have a mass of the order of 10^{20} protons with HFS pellets being a factor of ≈3 smaller than LFS pellets due to erosion in the much longer guiding tube. The injector was originally developed for the ASDEX Experiment [25] and only recycled at W7-X. Therefore, the pellet size was not chosen but rather given and could not be altered easily. Nevertheless, the plasma volume of ASDEX ($14\,\mathrm{m^3}$) is comparable to W7-X ($30\,\mathrm{m^3}$) and the injector was a good compromise to start preliminary experiments, before the ITER-like steady state injector was available, which is capable to produce pellets of 2…3 mm size with 10 Hz repetition frequency and up to $1000\,\mathrm{m\,s^{-1}}$ velocity. The peripheral diagnostics of the injector collect data on the injection time and side, the pellet mass and velocity (microwave cavity de-tuning by the pellets once they fly through it) as well as ablation radiation (fast PIN-photodiode, bandwidth 1 MHz) and hence penetration depth [6]. Radially resolved electron density (n_e) and temperature (T_e) measurements are performed by an incoherent TS diagnostic [26]. It provides profile measurements containing 42 data points spread across the ≈1.2 m plasma diameter and island region at a toroidal angle of $\Phi = 171.2^\circ$. It is able to operate in two modes a) the 'Standard-Mode' featuring a fixed 30 Hz repetition frequency and b) the 'Burst-Mode' repetitively (every 200 ms on average) providing short (1.1 ms) bursts of 10 kHz measurements, which can be synchronized to occurring events [19]. The interferometry diagnostic [27] sharing a line of sight with the TS system delivers line integrated

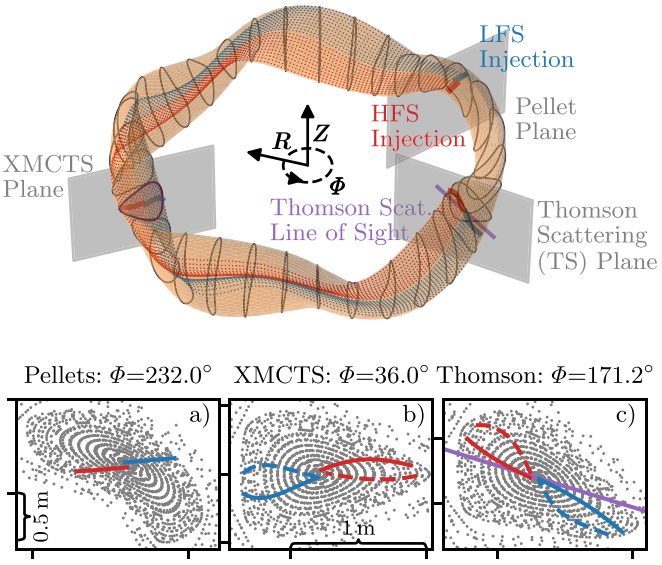

Figure 1. 3D plot of the pellet injection flight path (red for HFS injection, blue for LFS injection) within the last closed flux surface across the toroidal plasma (orange) mapped to different locations in the poloidal plane of the XMCTS and the TS diagnostic shown for the magnetic 'standard configuration'. Subfigure (*a*)–(*c*) show the mapped paths for the shortest magnetic connection in positive (solid line) and negative (dashed line) toroidal rotation in front of a Poincaré map (grey). The purple line in (*c*) indicates the beam path of the TS lasers.

density data ($\int n_e \mathrm{d}\ell$) with a sampling frequency in the kilohertz range.

The W7-X XMCTS diagnostic is able to provide 2D Gaussian process inverted [28, 29] x-ray emission tomograms of the plasma at a toroidal angle of $\Phi = 36.0^\circ$. X-ray emission might originate from bremsstrahlung, continuum radiation, recombination or line radiation, depending on the plasma conditions and hence location within the plasma [30]. For nearly fully ionized hot plasma regions, the contribution of the bremsstrahlung dominates the signal. Its total radiated power P is proportional to n_e, T_e and the effective ion charge Z_{eff} with different contributions:

$$P \propto Z_{\mathrm{eff}} n_e^2 T_e^{1/2}. \tag{1}$$

Consequently, a change in electron density has a much larger effect on the radiated power than a change in electron temperature.

The different toroidal and poloidal positions of the pellet injector, the TS and the XMCTS diagnostic are shown in figure 1. To analyze and compare the collected data, the designed pellet injection flight path was mapped to the poloidal planes of the diagnostics using fieldline tracing [31] and the 'VMEC2000' code [32]. Figures 1(*a*)–(*c*) show the results of this mapping procedure exemplary for the shortest magnetic connection in positive (solid line) and negative (dashed line)

toroidal rotation direction. To be able to compare data collected from different diagnostics at different toroidal locations with different shapes of the magnetic cage, magnetic coordinates were introduced in VMEC2000: the toroidal angle Φ is the same as in cylindrical coordinates shown in figure 1, Θ denotes the poloidal angle in the poloidal plane (e.g. in figures 1(*a*)–(*c*)) and the normalized toroidal magnetic flux enclosed by the corresponding flux surface is denoted by s. In the case of circular flux surfaces $s \approx (r/\langle r_{\mathrm{LCFS}}\rangle)^2$ with r being the minor radius coordinate of the torus. Flux-surface equilibria are assumed in VMEC2000 coordinates, which means plasma parameters on all poloidal shells of equal $|s|$ are equal. In our specific study, we observe fast phenomena on time scales faster than flux-surface equilibria are reached. To distinguish between the part of the TS profile on the inboard side or HFS of the torus and the part of the TS profile on the outboard side or LFS of the torus, the definition of s was altered, such that TS data from the HFS was denoted by a negative s and TS data from the LFS was denoted by a positive s in the mapping process.

An XICS diagnostic is installed at W7-X at a toroidal angle of $\Phi = 159.0^{\circ}$. After a tomographic inversion [33], it provides T_{i} and E_{r} profiles. The plasma Energy or diamagnetic Energy of the plasma W_{dia} is directly related to the toroidal magnetic flux, which is measured by three diamagnetic loops at W7-X, located at different toroidal angles with different poloidal cross-sections [34].

2.2. W7-X pellet injection database

Earlier pellet fueling experiments in large stellarators and heliotrons found central fueling mechanisms based on plasma particle transport [35–37]. Those experiments usually focused on certain pellet series or individual pellets and the corresponding plasma background parameters. In this study, both an analysis of individual pellets as well as a statistical analysis of more than 1000 pellet events in W7-X were carried out, to analyze the pellet ablation and deposition process as well as the subsequent fast transport. To apply statistical methods to identify actuators for efficient pellet core fueling, a database containing relevant pellet properties (i.e. mass, velocity, number in series, injection side, frequency, penetration) and background plasma parameters (i.e. magnetic configuration, heating, other fueling, density, electron and ion temperature, radial electric field, diamagnetic energy, impurities) was set up. Whenever available, the pre- and post-pellet-injection plasma parameters were included to analyze their alteration.

3. Experimental results

Pellet injection involves a three-step process of ablation, deposition and transport/diffusion. Given the fundamentally different physics mechanisms involved, the three phases are discussed separately to gain a better understanding how they might affect the core-fueling success and to identify possible markers of it. We are well aware of the fact that these three phases will interfere with each other in the experiment, in the spatial as well as in the time domain.

3.1. Ablation

The ablation of the pellet material leads to the formation of a neutral ablation cloud. The cloud shields the pellet from further impinging plasma electrons and hence extending the penetration of the pellet before its full evaporation as described by the Neutral Gas Shielding (NGS) model [7]. Given that the fueling of the plasma core is the primary focus of our analysis, the ablation is investigated using our pellet database with regards to the penetration depth only.

The relation between the measured pellet penetration depth:

$$\lambda_{\mathrm{Exp.}} = v_{\mathrm{pellet}} \cdot t_{\mathrm{H}_\alpha}, \tag{2}$$

as product of pellet injection velocity & the duration of the H_α ablation-light emission and the pellet penetration depth predicted by the NGS model (λ_{NGS}) is shown in figure 2(*a*).

Typical penetration depths of $20\ldots40\%$ and $40\ldots60\%$ of the minor plasma radius for HFS and LFS pellets respectively were measured. The difference in penetration depth is mainly caused by the difference in pellet size. The erosion of the HFS pellets within the guiding tube is a factor of 2–3 larger, due to the longer transfer distance. As a consequence, the HFS pellets are usually lighter than the LFS pellets by this factor and therefore HFS and LFS pellets are mostly represented by the purple and yellow markers respectively. Although following the general trend, the experimentally found penetration was systematically deeper for LFS pellets compared to the NGS model.

To investigate the discrepancy to the purely analytical model, we compare to a more heuristic model of the penetration depth provided by Parks and Turnbull [38] and Baylor *et al* [39]. It is based on a parameterized adaption of the NGS model to the International Pellet Ablation Database (IPAD). The model predicting the penetration depth λ_{IPAD} reads:

$$\frac{\lambda_{\mathrm{IPAD}}}{\langle r_{\mathrm{LCFS}}\rangle} = C \cdot \frac{T_{\mathrm{e}}}{[keV]}^{a} \cdot \frac{n_{\mathrm{e}}}{[1\times10^{20}\mathrm{m}^{-3}]}^{b} \cdot \frac{m_{\mathrm{p}}}{[1\times10^{20}\mathrm{atoms}]}^{c} \cdot \frac{v_{\mathrm{p}}}{[\mathrm{m\,s}^{-1}]}^{d} \tag{3}$$

The freely optimizable parameters C, a, b, c and d allow to compare experimental data to the analytical parameters of the NGS model which can be found in the first line of table 1. The parameters weight the contribution of the central plasma electron temperature T_{e}, central density n_{e}, pellet mass m_{p} and pellet velocity v_{p} on the penetration depth.

The IPAD model parameters for W7-X were determined by a non-linear least square fit [40] to the experimental data. The parameters delivered from this fit of the heuristic model to

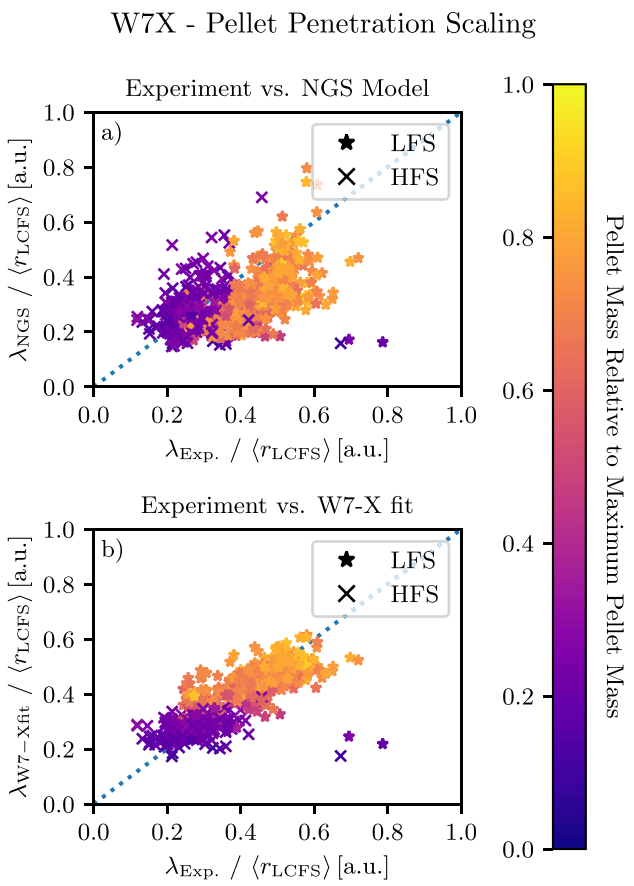

Figure 2. Comparison of the measured pellet penetration depth $\lambda_{\mathrm{Exp.}}$ and the prediction by (*a*) the NGS model λ_{NGS} and (*b*) the W7-X fitted IPAD regression model $\lambda_{\mathrm{W7-X\,fit}}$.

Table 1. Comparison of NGS model parameters to parameters determined by fitting the heuristic (IPAD) model to the W7-X experimental data and the original IPAD parameters from [39].

parameter	C	$a(T_e)$	$b(n_e)$	$c(m_p)$	$d(v_p)$
NGS	0.079	−0.56	0.11	0.19	0.33
W7-X fit	0.050	−0.13	0.07	0.45	0.39
IPAD	0.079	−0.51	−0.03	0.12	0.32

the experimental penetration depth can be found in the second line of table 1. To validate the quality of this fit model, a comparison of the penetration depth $\lambda_{\mathrm{W7-X\,fit}}$ gained via applying the fitted parameters to the heuristic IPAD model from equation (3) to the experimentally determined penetration depth $\lambda_{\mathrm{Exp.}}$ is shown in figure 2(*b*). The predicted and measured penetration depths match quite well, given the numerous uncertainties (scattering injection angle, erosion in the tube, changing velocity, ...). The analysis revealed a weaker plasma temperature and stronger pellet mass dependency than predicted by the NGS model, but it needs to be acknowledged that triangular T_e and n_e profiles are assumed by both the NGS and IPAD model, which is only a rough estimate of the real situation in W7-X. The W7-X fit dependency on the plasma density however matches better to the NGS model than the respective parameter from the original IPAD scaling [39].

3.2. Deposition

The deposition of the pellet material as result of the expansion and movement of the pellet material which was firstly ablated and secondly ionized by the background plasma particles can be calculated via pellet injection codes like HPI2 [41]. The quality of these predictions are limited by the considered physics mechanisms. The HPI2 code was developed for tokamaks and later adapted for the use in stellarators [42]. The main drift mechanism embedded in HPI2 is the $\boldsymbol{E}_{\nabla B} \times \boldsymbol{B}$ - drift. It is always directed towards lower magnetic field strength.

Table 2. HPI2 simulation results of the radial $\boldsymbol{E}_{\nabla \mathrm{B}} \times \boldsymbol{B}$ - drift velocities and plasmoid dimensions (range from the beginning to the end of homogenization phase) for typical W7-X plasma conditions and pellets injected from LFS and HFS.

	LFS	HFS
$\langle v_{\boldsymbol{E}_{\nabla \mathrm{B}} \times \boldsymbol{B}} \rangle$	$1.4 \ldots 3.9 \times 10^3 \mathrm{m\,s^{-1}}$	$0.7 \ldots 4.1 \times 10^3 \mathrm{m\,s^{-1}}$
r_{radial}	$0.02 \ldots 0.40\,\mathrm{m}$	$0.01 \ldots 0.18\,\mathrm{m}$
r_{poloidal}	$0.02 \ldots 0.02\,\mathrm{m}$	$0.01 \ldots 0.02\,\mathrm{m}$
r_{toroidal}	2.8...25 m	

In axisymmetric tokamaks this is always pointing radially outwards, in the complex 3D-shape of stellarators this is not always the case. Depending on the injection location (HFS vs. LFS) as well as the toroidal extension of the plasmoid, the drift direction and velocity varies. For simplicity, usually $\langle v_{\boldsymbol{E}_{\nabla \mathrm{B}} \times \boldsymbol{B}} \rangle$ of the $\boldsymbol{E}_{\nabla \mathrm{B}} \times \boldsymbol{B}$ - drift velocity for the $\langle r_{\mathrm{toroidal}} \rangle$ of the toroidal expansion of the plasmoid is used. A scan of the radial $\boldsymbol{E}_{\nabla \mathrm{B}} \times \boldsymbol{B}$ - drift velocities as well as plasmoid dimensions (range from the beginning to the end of homogenization phase) for typical W7-X plasma conditions was conducted via HPI2 for pellets injected from LFS and HFS. The results are shown in table 2.

For a pellet injected to W7-X in typical plasma conditions, the radial displacement from the $\boldsymbol{E}_{\nabla \mathrm{B}} \times \boldsymbol{B}$ - drift would be $\sim \mathcal{O}(5 \ldots 7.5\,\mathrm{cm})$ at the end of the homogenization phase [43].

To discuss the deposition of the pellet material based on experimental data, information of both electron temperature T_e and density n_e is necessary. At first 2D tomographic data from the x-ray emission tomography is shown in figure 3 where density and temperature information cannot be decoupled, because they both affect the total radiated x-ray power as discussed in section 2.1: in theory, the contribution from a lower temperature to the radiation could be compensated by the higher density's contribution to the radiation - under consideration of the different scalings from equation (1). For this reason, profiles of T_e and n_e as well as line-integrated density data is later individually employed to validate and qualify the tomographic measurements.

For the analysis of pellet induced relative changes in the x-ray emission tomograms inversion time scales of 0.1 ms and length scales of 10 cm proved to be most robust. The technique is prone to produce artifacts along the line of sight of the specific cameras, if strong localized emitters (like pellet plasmoids) occur. Hence the tomograms can only provide a rough picture and only strong features are discussed further. However an advantage of this diagnostic is, that the data after inversion is available at ~10 kHz continuously. The radiation outside the contained plasma region ($s = 1$, indicated by the solid gray line in the tomograms) was not analyzed.

In figure 3 the relative change in the x-ray emission tomograms introduced by a pellet injected from the HFS (subfigures column *I*) and two pellets injected from the LFS (subfigures columns *II* and *III*) in W7-X program 20180918.047 at 2.2129 s, 2.2465 s and 2.9739 s after the start of the plasma heating are shown respectively. The subtracted reference tomogram was selected for each pellet at $t_{\mathrm{injection}}$, which is when the H_α ablation emission from the respective pellet reached 10% of its peak value. Firstly (subfigures (*a*) in the upper row) the ablated and subsequently ionized pellet material forms multiple so called 'plasmoids', which all together (not individually) can be identified as blob of increased radiation at the locations expected via the mapping of the pellet flight path into the XMCTS plane (= nock of the black arrows: right corner for HFS pellets, upper left corner for LFS pellets). On the timescale of about 1.2 ms in case *I*), 0.8 ms in case *II*) and 0.7 ms in case *III*), these particles rotate in the counter-direction of Θ around the plasma core (clockwise in subfigures (*b*) in the middle row and subfigures (*c*) in the lower row), indicated by the black arrows. This observation cannot be explained by the $\boldsymbol{E}_{\nabla \mathrm{B}} \times \boldsymbol{B}$ - drift. The displacement is much larger and not directed radially outwards as expected for the $\boldsymbol{E}_{\nabla \mathrm{B}} \times \boldsymbol{B}$ - drift, but it can be explained by another plasma drift: the existence of plasmoids which disturb the flux surface equilibrium of plasma temperature and density makes it possible to directly observe the poloidal $\boldsymbol{E}_\mathrm{r} \times \boldsymbol{B}$ - drift rotation of the plasma via the x-ray emission tomography. The rotation velocity observed in the poloidal plane in figure 3 is the result of the toroidal background $\boldsymbol{B}$ - field and the radial electric field $\boldsymbol{E}_\mathrm{r}$. The rotation converged in all analyzed pellet series to an almost constant value typically after 5–15 pellets were injected. The change in the radial electric field at half radius $\boldsymbol{E}_\mathrm{r}$ throughout all pellet series shows the same converging behavior. In a toroidal plasma configuration like W7-X, the $\boldsymbol{E}_\mathrm{r} \times \boldsymbol{B}$ - drift results in a poloidal rotation of the background plasma independent from the $\boldsymbol{E}_{\nabla \mathrm{B}} \times \boldsymbol{B}$ - drift of the plasmoid. The $\boldsymbol{E}_\mathrm{r} \times \boldsymbol{B}$ - drift rotation velocity:

$$v_{\boldsymbol{E}_\mathrm{r} \times \boldsymbol{B}} = \frac{\boldsymbol{E}_\mathrm{r} \times \boldsymbol{B}}{B^2}, \tag{4}$$

is a function of the plasma magnetic and electric fields.

The evolution we found in the tomograms was not introduced by multiple passes of propagation of the plasmoid particles along the flux tube in toroidal co- and counter- directions within the initial plasmoid flux tube, because in this case, one would find blobs appearing on the tomograms in various locations on the given flux surface of the plasmoid - depending on the rotational transform - rather than a smooth rotation. Also, the maximum toroidal extension of the plasmoids found via our HPI2 simulations was 25 m which is less than the 35 m toroidal circumference of W7-X. The ablation process described in the previous section is proceeding throughout the depicted time interval. As such, the ablation is continuously

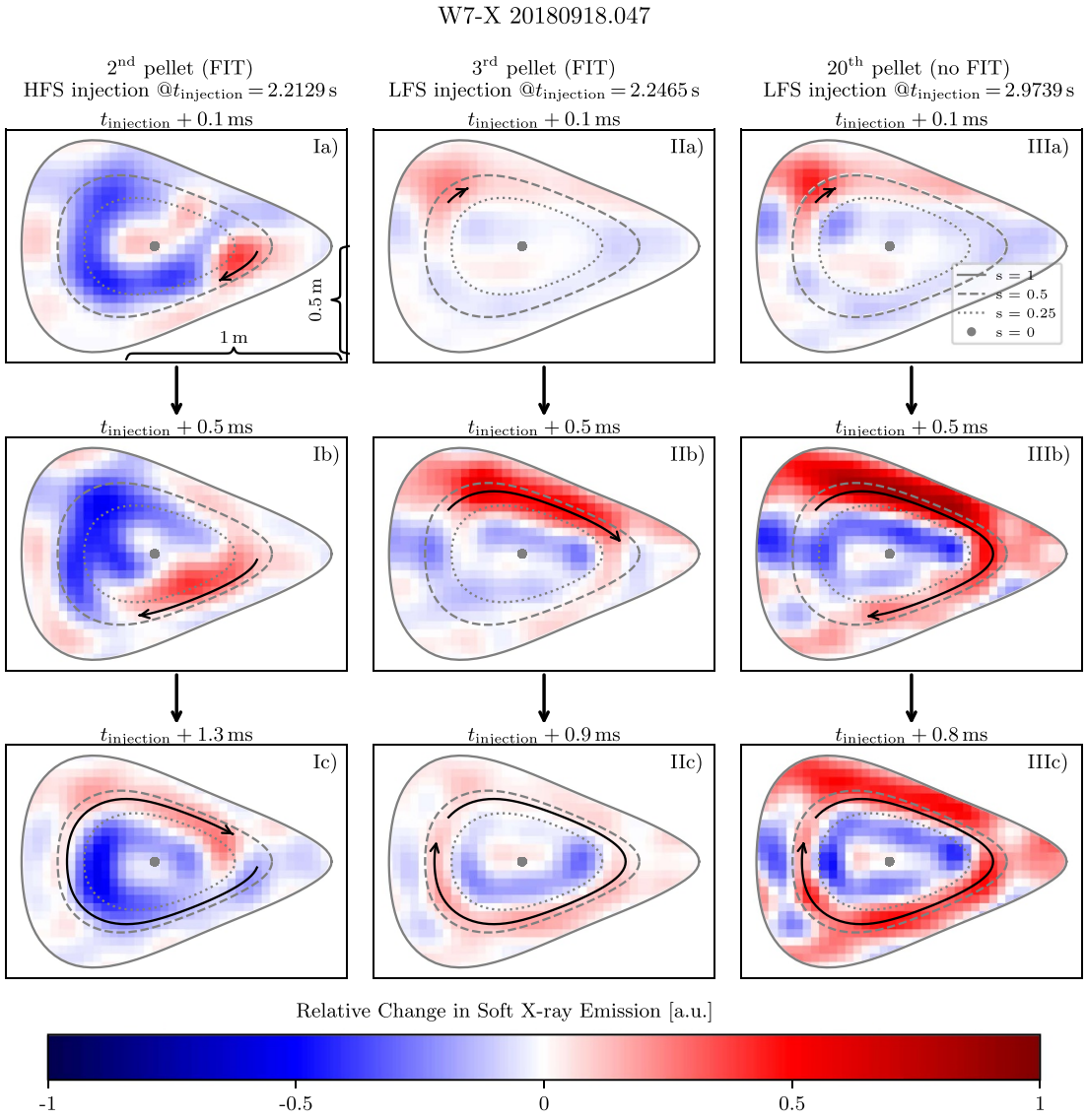

Figure 3. Real space 2D Gaussian process inverted x-ray emission tomograms of the plasma poloidal plane at $\Phi = 36°$ in experimental program 20180918.047 during the injection of a pellet series. The relative change after (*a*) 0.1 ms, (*b*) 0.5 ms and (*c*) 1.3 ms/0.9 ms/0.8 ms compared to the last unperturbed measurement just before the injection of the pellet is displayed. The black arrows were added to indicate the drift of the pellet material. Case *I*: 2nd pellet injected from HFS at $t = 2.2129$ s and $\int n_e \, d\ell = 6.5 \times 10^{19}\,m^{-2}$, $t_{ablation} = 0.66$ ms. Case *II*: 3rd pellet injected from LFS at $t = 2.2465$ s and $\int n_e \, d\ell = 7.0 \times 10^{19}\,m^{-2}$, $t_{ablation} = 0.80$ ms. Case *III*: 20th pellet injected from LFS at $t = 2.9739$ s and $\int n_e \, d\ell = 1.3 \times 10^{20}\,m^{-2}$, $t_{ablation} = 0.87$ ms.

producing new plasmoids at the location of the pellet, while the predecessing plasmoids rotate further around the core and are still visible on the tomogram - in combination, the two processes might create the misleading impression of a large object rather than individual plasmoids rotating around the core. For the LFS injection (case *II* & *III*) this eventually leads to the entire flux shell at $s \approx 0.5$ is being filled with particles from the pellet after around 1 ms. In case *I*), in contrast to that, the blob containing multiple (all) plasmoids performs only half a poloidal turn before all material from the smaller HFS pellet was ablated, resulting in a 'Yin and yang'-like structure rotating further around the core (subfigures (*Ib*) and (*Ic*) of figure 3). The cases in figure 3 were selected because of their rather low absolute $\boldsymbol{E}_r$ - field and hence slow $\boldsymbol{E}_r \times \boldsymbol{B}$ - drift rotation velocity. Otherwise it would have been difficult to resolve the drift rotation in the tomograms due to a limitation of the temporal sampling for the Gaussian inversion. Apart from the rotating plasmoids, the x-ray emission in figure 3 is significantly reduced on a timescale of 0.5 ms almost all the way in to the core in all three cases, remaining like this for ≈5 ms.

The TS diagnostic, is able to measure both n_e and T_e individually. It was therefore used to complement the observations made via the XMCTS tomograms and to distinguish which change in the x-ray emission was introduced by a change in n_e and which by a change in T_e. A set of typical 10 kHz 'Burst-Mode' TS n_e and T_e profiles during a pellet injection

is shown in [19]. In the current study, the density and temperature change introduced by all 189 LFS pellets analyzed with the 'Burst-Mode' during the 1st millisecond after their injections were combined into one dataset and Gaussian process fitted jointly in the time and space domain, to reduce the statistical error in the TS data as well as the one produced by the bad reproducibility of the pellets. For this type of analysis, only the change in n_e and T_e is used, because the equilibrium density and temperature profiles were to different to allow for a combination. The result is shown in figure 4.

A dedicated delay is visible between the density increase on the two sides of the profile, which are represented by negative and positive s. The mean delay of ∼0.2 ms corresponds to the duration of half a poloidal $\boldsymbol{E}_r \times \boldsymbol{B}$ - rotation of the pellet plasmoids. This is the time the LFS plasmoids typically need to cross the line of sight of the TS system first on the HFS (negative s) and second on the LFS (positive s) of the torus. As shown in figure 1(c) a LFS-pellet plasmoid would at first miss the LFS-side of the Thomson-Scattering line of sight given the magnetic topology. Taking into account the counter-clockwise direction of the poloidal $\boldsymbol{E}_r \times \boldsymbol{B}$ - drift rotation, the plasmoids will cross the line of sight at the HFS first, and after half of a period of rotation cross the line of sight at the LFS side, as it is visible in figures 4 and 5. The ∼0.2 ms mean delay can be identified even better comparing the relative change in electron density only at the location of the peak density increase for both sides of the profile in figure 5(b).

Figures 4(b) and 5(b) show only the mean delay because they combine all available LFS pellets. It is possible to estimate the mean $\boldsymbol{E}_r$ from equation (4) using the ∼0.2 ms mean delay and the circumference of the $\boldsymbol{E}_r \times \boldsymbol{B}$ - drift rotation in ion root direction. Taking the toroidal background magnetic field of $B = 2.7$T and a circumference of 1.6 m at $s = 0.7$ together with the ∼0.2 ms mean delay, the mean electric field E_r would be $\sim -21.6\,\mathrm{kV\,m^{-1}}$. This matches the $\boldsymbol{E}_r$ measurements from the XICS diagnostic. Individual delays could be longer or shorter depending on the individual $\boldsymbol{E}_r$ as discussed later on a specific pellet series.

After all pellet material was ablated and ionized, the equilibration of emission on the flux shell at $s \approx 0.5$ observed in the 2D tomograms is seen in the TS profiles as well, implied by the symmetric perturbation at the same flux coordinate. The electron density profiles of the HFS-injected pellets show the same behavior (with flipped sides, as expected), but due to the smaller number of HFS injections and the smaller HFS pellet mass, the noise in the data is much higher and therefore only the LFS cases are shown. The combined line-integrated density signal (black, $\int n_e \mathrm{d}\ell$) from the 189 LFS pellet injections as measured by the interferometer was plotted on top of the 2D electron density heat map in 4(b), together with the line integral of the electron density gained from TS (blue). These signals match very well too. Moreover, the median duration time of the H_α ablation emission from the same set of pellets was 0.67 ms, matching the raise time of the line-integrated density signal in figure 4(b).

The line integrated density signal of individual pellets shows a 'bell-like ringing' (damped oscillation) for most HFS pellets and some smaller LFS pellets, before the material has

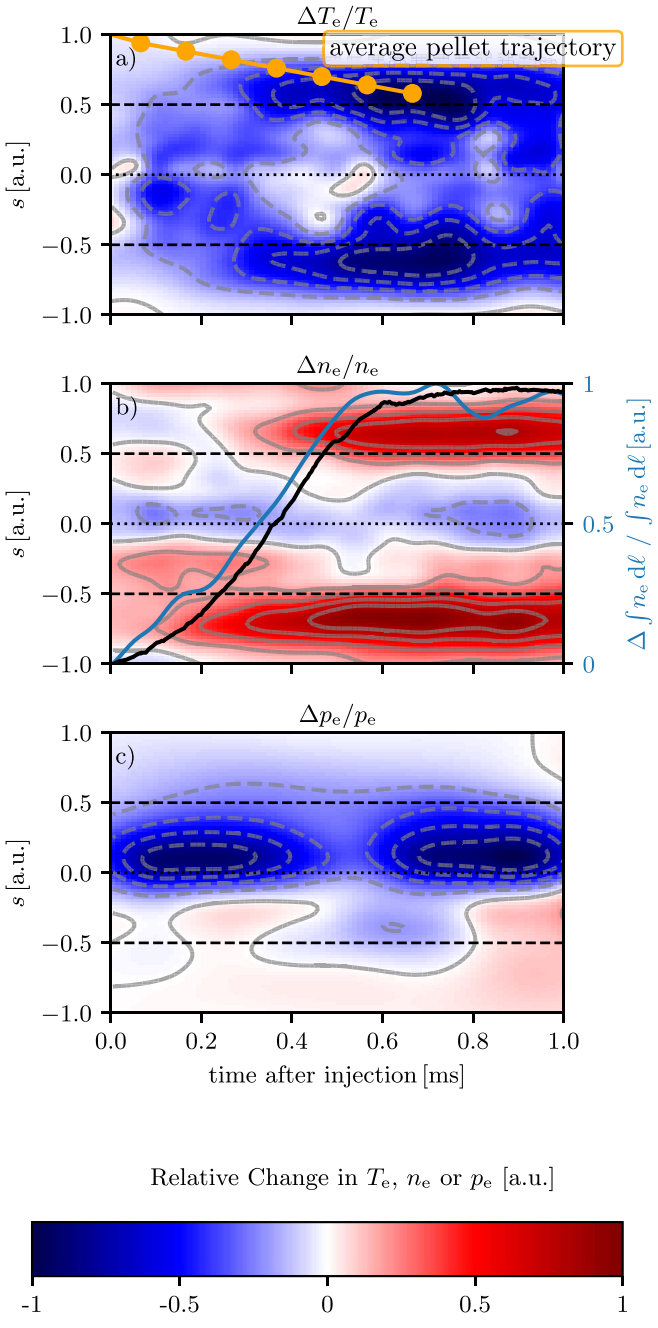

Figure 4. Relative change in (a) electron temperature, (b) electron density and (c) electron pressure relative to the pre-pellet plasma conditions. The 'Burst-Mode' TS data from 189 individual pellets injected from LFS was combined into one data set (eleven differential profiles per pellet) and Gaussian regression process fitted jointly in the time and space domain. In subfigure (b) the relative change in the line-integrated density from the interferometry diagnostic combining the 189 pellets was plotted in black and the line integral of the radial TS density profiles in blue for comparison on the second y-axis. The average trajectory (penetration vs. time) of the pellets is shown exemplary in subfigure (a). It ends with the full ablation of all pellet material at $s = 0.58$ after 0.666 ms (median values of the 189 individual pellets).

equilibrated on the flux shell, as exemplary shown in figure 6. This is because the HFS pellets usually do not fill up the full shell due to their smaller mass and cross the interferometry

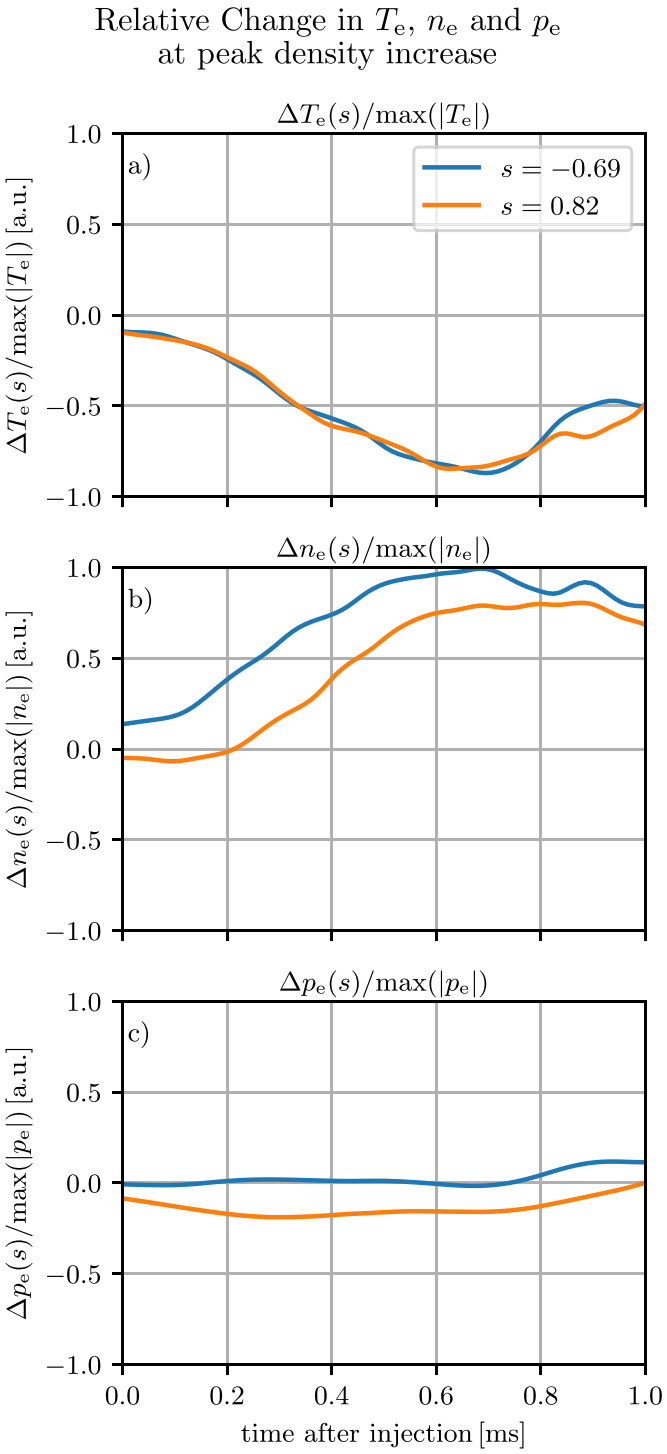

Figure 5. Relative change in (*a*) electron temperature, (*b*) electron density and (*c*) electron pressure relative to the pre-pellet plasma conditions at the location of the peak density increase from figure 4.

line of sight multiple times before equilibration on the flux surfaces, as already discussed in the context of figures 3(*Ib*) and (*Ic*) ('Yin and yang'-like structure). The oscillation frequency gained from the signal in figure 6 of ≈ 333 Hz (plasmoid crossing the line of sight twice for one poloidal rotation) matches

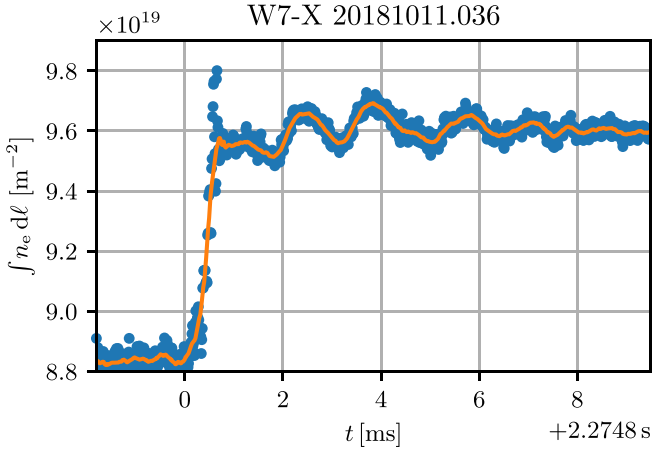

Figure 6. Line integrated electron density signal after the 2nd pellet injected from HFS to W7-X experimental program 20181011.036 at $t = 2.2748$ s. The orange line is a 30-samples moving average to guide the eye of the reader.

the frequency calculated from the $\boldsymbol{E}_r \times \boldsymbol{B}$ - drift within the error margins using $\boldsymbol{E}_r$ from the XICS diagnostic.

Figure 4(*a*) shows the relative change in electron temperature, introduced by the 189 LFS pellets and 5(*a*) shows the same at the location of peak density increase. As opposed to the density, the cooling introduced by the pellets reaches deep into the plasma core on a timescale of 0.5 ms and is virtually symmetric. Hence, the cooling propagates independent from the particles. The pressure in figure 5(*c*) shows only a weak change at those radial locations, but a rather immediate decrease at the plasma core in figure 4(*c*), which is not understood yet.

Combining the observations from the x-ray tomograms and the TS profiles we draw the general conclusion, that the pellet particles remain at $s \approx 0.5$ and rotate in the poloidal plane while the cooling effect is decoupled from the particles and quickly reaches the plasma core.

Although W7-X is a non-axisymmetric device, there are to date no diagnostics which could be used to analyze the 3rd dimension i.e. the toroidal component of the pellet cloud dynamics, which could therefore only be discussed on basis of the W7-X magnetic field topology.

Due to the central energy deposition of the electron cyclotron resonance heating (ECRH) [44], typically the radial electric field $\boldsymbol{E}_r$ is positive ('electron root' [45]) in the plasma core and negative towards the plasma edge in W7-X. The sign usually flips at $0.3 < s < 0.5$ and in many cases the size of the gradient significantly increases at $s \approx 0.5$. As a consequence of the injection of pellets however, the core $\boldsymbol{E}_r(s \lessapprox 0.5)$ is usually strongly reduced and even flips sign ('ion root')[46]. This is seen in figure 7(*a*). The core radial electric field is positive in the pre-pellet phase and then flips sign. This transition into the ion root regime is often observed in pellet injection discharges. After the end of the pellet series, $\boldsymbol{E}_r$ typically recovers towards its pre-pellet profile within 1 . . . 2 s (several energy confinement times).

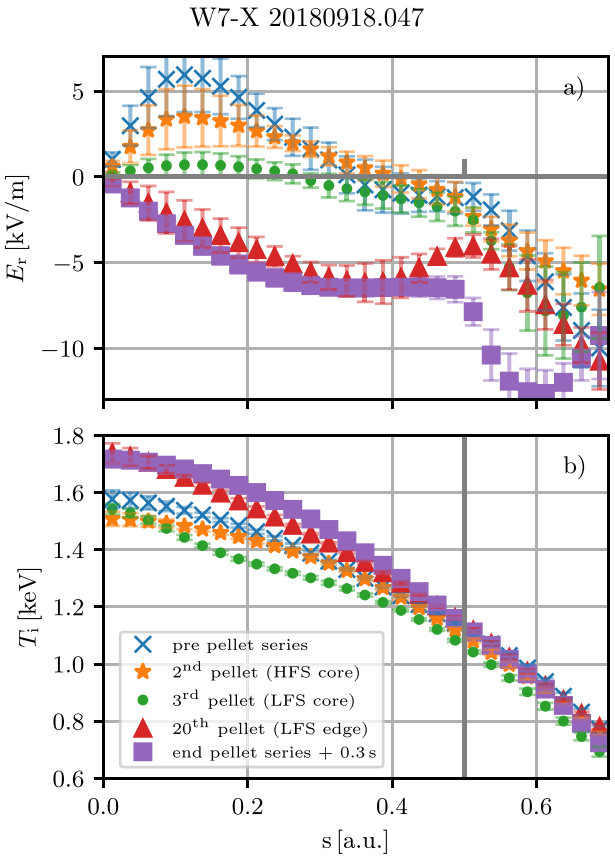

Figure 7. Profile change of the radial electric field $\boldsymbol{E}_r$ and Ion Temperature T_i during a series of pellets injected in experimental program 20180918.047 observed via the XICS diagnostic. For $s > 0.7$ the signal-to-noise ratio (SNR) becomes too low for reliable measurements. The related $\int n_e \, d\ell$ was: $6.2 \times 10^{19}\,m^{-2}$ before the start of the pellet series, $6.5 \times 10^{19}\,m^{-2}$ before the 2nd pellet, $7.0 \times 10^{19}\,m^{-2}$ before the 3rd pellet, $1.3 \times 10^{20}\,m^{-2}$ before the 20th pellet and $1.4 \times 10^{20}\,m^{-2}$ at the end of the pellet series +0.3 s.

The $\boldsymbol{E}_r \times \boldsymbol{B}$ - drift rotation direction observed after pellet injection via the x-ray emission tomograms in figure 3 is consistent with the ion-root confinement indicated by the data in figure 7(*a*). The $E_r(s = 0.7) = -7 \ldots -12 kV m^{-1}$ gained from the XICS diagnostic for the three pellets and the calculation via the $\boldsymbol{E}_r \times \boldsymbol{B}$ - drift rotation period taken from figure 3 (1.4…0.8 ms) delivering $E_r(s = 0.7) = -6.2 \ldots -10.8 kV m^{-1}$ agree very good as well, supporting the assumption that the rotation of the pellet material visible in figure 3 was caused by the $\boldsymbol{E}_r \times \boldsymbol{B}$ - drift. The calculation of E_r for the individual pellets was performed the same way as for the 189 combined pellets with the ∼0.2 ms mean delay on the Thomson density data in figure 4(*b*) an 5(*b*).

3.3. The FIT-effect: fast inward directed radial particle transport

The fully evaporated and ionized pellet material equilibrates on the flux surfaces (seen as a 'ring' on the 2D tomograms) at $s \approx 0.5$ typically after ≈5 ms (depending on the individual rotation velocity). Subsequently, for both HFS & LFS injection geometries central accumulation of plasma particles was observed on timescales of $\mathcal{O}(10\,ms)$ which cannot be explained by neoclassical transport or diffusion. This fast inward directed particle transport (FIT) effect can be identified on the XMCTS tomograms in figure 8.

In case *I*) (injection of the 2nd pellet in program 20180918.047 from HFS) the core radiation started rising after ≈9 ms as shown in subfigure (*Ie*) of figure 8. After ≈30 ms the increase in core radiation was well established, as can be seen in subfigure (*If*), while the radiation at the location of the former deposition flux shell decreased back to pre-pellet levels. The exact same behavior was observed for the 3rd pellet in program 20180918.047 (subfigures in the *II* column). It needs to be emphasized, that this pellet was injected from the LFS. In the third case (subfigures in the *III* column) for the 20th pellet in program 20180918.047 injected from LFS however, the core radiation did not increase. Only the reduction of emission caused by the core plasma cooling as discussed in section 3.2 can be observed. Ultimately, the emission on the deposition flux shell fades to near pre-pellet levels after ≈30 ms. As shown, the FIT-effect did not only occur with HFS pellets, but can also be observed for LFS injections. A missing FIT as well was not exclusively dedicated to LFS pellets, some HFS injections were missing it as well. Therefore, we were searching for other actuators and trends in the aforementioned pellet-plasma-parameter database as presented in section 4.

For the longer timescale of ≈30 ms no pellet-synchronized TS mode with multiple unperturbed post-pellet measurements is available. Yet the pellet injection frequency itself was usually about 30 Hz. To still evaluate the temporal evolution analogous to figure 4, it was made use of the unsynchronized timing between TS and pellet injection: the post-pellet TS measurements were randomly conducted immediately after a pellet injection or up to 33.3 ms later. As a consequence, combining the 380 pellets injected from LFS in total and observed with the 30 Hz 'Standard-Mode', the overall density and temperature evolution over all 380 could be reconstructed on this timescale. Beside mixing all 380 pellets, the caveat of this method was, that also the trigger-moment of the pre-pellet measurements were conducted randomly (more precisely always 33.3 ms before the post-pellet measurement) while consecutive pellet injections had about the same time increment given the 30 Hz injection frequency and also the effect observed takes place on the same timescale. Therefore, the pre-pellet 'equilibrium' measurement could be disturbed

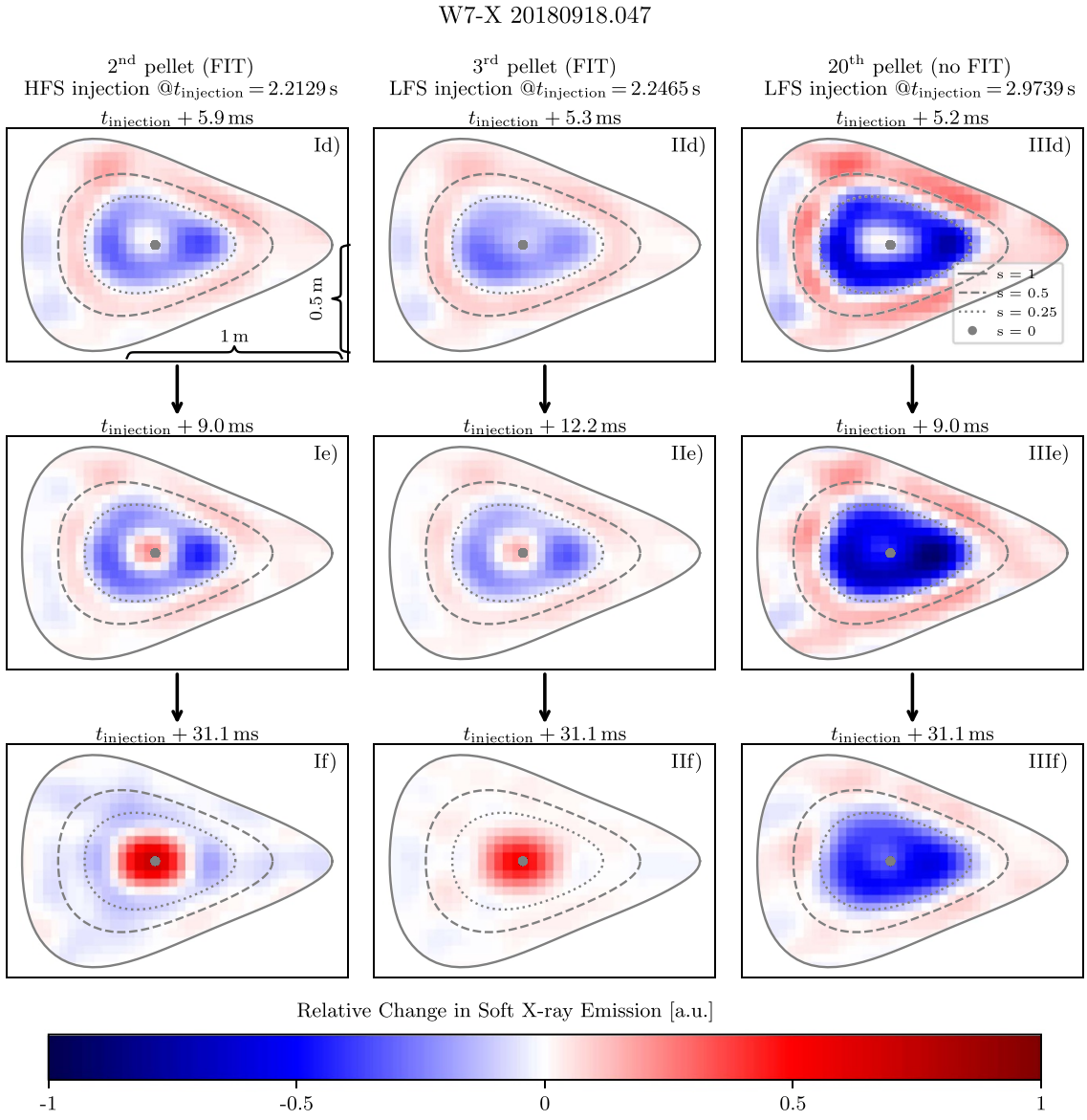

Figure 8. Real space 2D Gaussian process inverted x-ray emission tomograms of the plasma poloidal plane at $\Phi = 36^\circ$ in experimental program 20180918.047 during the injection of a pellet series. The relative change after (*d*) ≈5 ms, (*e*) ≈10 ms and (*f*) ≈30 ms compared to the last unperturbed measurement just before the injection of the pellet is displayed. Case *I*: 2nd pellet injected from HFS at $t = 2.2129$ s and $\int n_e \, d\ell = 6.5 \times 10^{19}\,\mathrm{m}^{-2}$. Case *II*: 3rd pellet injected from LFS at $t = 2.2465$ s and $\int n_e \, d\ell = 7.0 \times 10^{19}\,\mathrm{m}^{-2}$. Case *III*: 20th pellet injected from LFS at $t = 2.9739$ s and $\int n_e \, d\ell = 1.3 \times 10^{20}\,\mathrm{m}^{-2}$.

by the predecessor pellet: the closer the measurement ensued the pellet, the stronger was the disturbance. To raise awareness for this problem, a yellow overlay was put above the plots in figure 9 which horizontally fades out over increasing time.

In the density profile data in figure 9(*b*), the torus shell with increased density introduced by the pellet particles can be found as horizontal 'humps' as a direct continuation of figure 4(*b*). These density humps generally depleted on a timescale of the order of $\sim\mathcal{O}(10\,\mathrm{ms})$. Because not only FIT-effect cases were selected for this plot, but all available data, some material over time remains at $s \approx 0.5$ representing unsuccessful (e.g. no FIT) cases like case *III*) in figure 8. But even including these data points, fast central density accumulation is clearly visible on the said timescale.

Figure 9(*a*) shows a persistent reduction in core temperature over this timescale. This again rules out a fast central restoration of the core electron temperature as cause for the increased central x-ray emission in figure 7 case *I*) and *II*).

While not shown here, the Z_{eff}-profiles did only change marginally throughout a whole pellet series and almost negligible for a single pellet injection. Consequently, the fast density and x-ray emission increase was introduced by fueling pellet particles rather than an accumulation of impurities.

In an analysis published elsewhere [37, 47], we found that peaked density profiles are beneficial for good confinement/high performance plasma conditions. The described core fueling by single pellets results in a rather strong density profile peaking throughout a series of typically 30 pellets

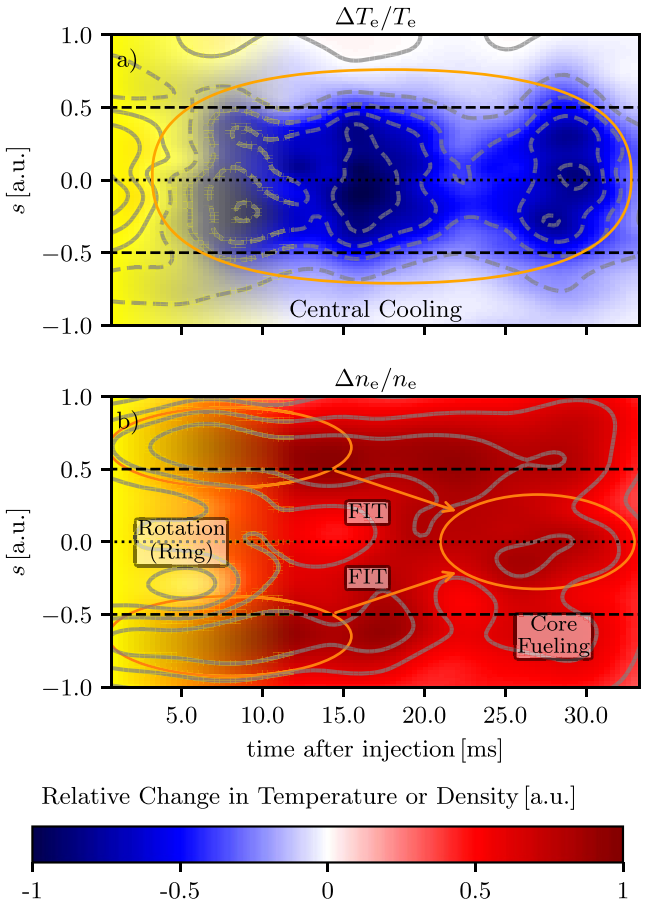

Figure 9. Relative change in (*a*) electron temperature and (*b*) electron density relative to the pre-pellet plasma conditions. Data collected shortly after the injection might be altered by the predecessor pellet (because no pellet-synchronized mode was available for this timescale) which is indicated by the yellow overlay. The TS data from 380 individual pellets injected from LFS (one differential profile per pellet) was combined into one data set and Gaussian regression process fitted jointly in the time and space domain. The orange annotations were added to guide the eye of the reader.

in W7-X. Core fueling via the FIT-effect was achieved by both LFS (35% FIT rate) and HFS (54% FIT rate) pellets within the whole database. A statistical analysis of these cases compared to the unsuccessful ones will be presented in section 4 to gain a better understanding of the appearance of the FIT-effect and the actuators potentially affecting this core fueling mechanism.

4. Statistical analysis of the parameters affecting the FIT-Effect

To test which plasma conditions or pellet parameters affect the FIT-effect, the distribution of core fueling pellets was compared to the distribution of non-core fueling (no FIT) pellets for several parameters. Unfortunately, no simple separation of two distinguished groups at a certain threshold was found for any analyzed parameter. E.g. no critical density was found for the bifurcation of FIT and no FIT cases in W7-X, while such a bifurcation was reported earlier for tokamaks [48]. Although we found general trends, it happened, that no FIT occurred at low densities and it was as well possible, that FIT occurred at higher density regimes and vice versa. Even if no FIT occurred to some predecessor pellets, a later one in the same series (at higher density) might again show FIT as well as the other way around. Therefore, the Mann–Whitney U hypothesis test introduced in the appendix was employed to test, whether a parameter is statistical relevant for the FIT-effect to occur. Pellet injections were identified as exhibiting the FIT-effect, when the Gaussian process regression fit of core $\Delta n_e(s = 0 \ldots 0.5)$ of two consecutive TS 'Standard-Mode' n_e profiles with a time increment of 33.3 ms was all positive. More than 20 plasma and pellet parameters were tested with some of them depending on each other. For example, the depth of the pellet penetration to the plasma is, among other parameters, a function of the duration of the ablation light emission. About half of the analyzed parameters were most likely affecting the appearance of the FIT-effect, according to the Mann–Whitney U test results ($z \gtrapprox 2, p \lessapprox 5$). On the other hand we could not find a significant influence for the magnetic configuration, the pellet velocity, the plasma density or the energy confinement time through the employed method. Despite the presence of various instabilities such as ITG, TEM or Alfvénic modes in W7-X [49–52], it is difficult to tell, which one is occurring in a specific experiment and whether or not it is relevant for the transport regime. The turbulent background in W7-X appears to be strongly broadband, and any identifiable mode signatures are typically embedded within it, with no clear temporal or spatial separation. This prevents definitive attribution of the FIT or no-FIT behavior to a particular instability or instability class. Even if mode signatures were isolated, it would require entirely separate, dedicated analyses to quantify their impact on plasmoid dynamics post-pellet injection; an effort which lies beyond the scope of the present work. Yet it is not unlikely, that TEM/ITG transport regimes influence the FIT vs. no FIT behavior, because the high performance operation regime reported in [37] and [47] are accompanied with core fueling/density profile peaking after pellet injection. In these publications, we analyzed and discussed the transport regimes and their interplay with pellet fueling for a few dedicated discharges. Nevertheless, no statistical significant correlation of the FIT effect and the normalized radial gradients of n_e, T_e, T_i or T_i/T_e was found analyzing the whole database in the course of the paper at hand.

In sections 3.2 and 3.3 we found, that after $1 \ldots 5$ ms both the HFS and LFS pellet material had equilibrated on the flux shell at $s \approx 0.5$, providing similar starting conditions for the FIT-effect. Therefore a combined analysis for all pellets was carried out on the 30 ms timescale. The results for all parameters, where z was greater than 1, can be found in table 3. For verification, an individual analysis for both injection geometries was performed as well. It widely agrees with the combined HFS & LFS results, but deviations will be addressed as well.

Table 3. Pellet and plasma parameters affecting core fueling success (FIT-effect) according to the Mann–Whitney U test. Commonly, a z-score of $z \gtrapprox 2$ (2 standard deviations) and p-value of $p \lessapprox 5\%$ are selected as sufficient significance levels. An effect size of $e < 0.1$ indicates a weak effect whereas an effect size of $e > 0.5$ indicates a strong effect. The signs of z and e denote unfavorable ($-$) and favorable ($+$) dependencies.

parameter	z	p [%]	e
$d_{\text{penetration}}$	1.2	22	0.12
$d_{\text{penetration}}$ (LFS only)	2.4	2	0.26
pellet no.[a]	−1.8	8	−0.17
$\varepsilon_{\text{fueling}}$	2.8	0.5	0.27
f_{pellet}[b]	1.1	29	0.10
W_{dia}	−2.2	3	−0.21
P_{ECRH}	−1.7	10	−0.16
$T_{\text{e}}(s \approx 1)$	−2.1	4	−0.20
$T_{\text{e}}(s \approx 0.5)$	−2.0	4	−0.19
$T_{\text{e}}(s \approx 0)$	−2.9	0.4	−0.28
$T_{\text{i}}(s \approx 1)$	−3.3	11	−0.32
$T_{\text{i}}(s \approx 0.5)$	−4.5	0.2	−0.43
$T_{\text{i}}(s \approx 0)$	−4.8	0.1	−0.46
$\beta(s \approx 1)$	−1.6	10	−0.16
$\beta(s \approx 0.5)$	−3.0	0.3	−0.29
$\beta(s \approx 0)$	−2.7	0.7	−0.26
$E_{\text{r}}(s \approx 1)$[c]	−2.9	28	−0.27
$E_{\text{r}}(s \approx 0.5)$[c]	−1.1	31	−0.11
$E_{\text{r}}(s \approx 0)$[c]	−1.79	83	−0.17

[a] 5th–10th LFS and 1st–7th HFS pellet most likely to trigger FIT-effect.
[b] Effective frequency (total count of successful pellets divided by pellet interval duration).
[c] Poor data quality.

4.1. Penetration depth

The FIT-effect seems correlated to the depth the pellet penetrates into the plasma, the so called penetration depth $d_{\text{penetration}}$, which can be calculated from the duration of the H_α ablation light t_{H_α} ($= t_{\text{ablation}}$) and the pellet velocity. For an analysis taking only the LFS pellets into account, a strong correlation was found ($z = 2.4$, $p = 2\%$, $e = 0.26$). However, the analysis for a combination of HFS and LFS pellets showed, if any, only a weak correlation and half the effect size ($z = 1.2$, $p = 22\%$, $e = 0.12$). The result that deeper penetration (positive sign of z and e) acts beneficial on the FIT-effect and hence fast fueling of the plasma core - in particular for LFS-injected pellets - drawn from the pellet database is very useful. It was neither possible to draw this conclusion from the XMCTS data nor the TS data alone due to its too low spacial or temporal resolution respectively.

4.2. Pellet number, fueling efficiency and radial electric field E_r

The global fueling efficiency $\varepsilon_{\text{fueling}} = \Delta \int n_e \mathrm{d}\ell / n_{\text{pellet}}$ and the FIT-effect are correlated as well ($z = 2.8$, $p = 0.5\%$, $e = 0.27$) which seems natural: pellet particles reaching the core are well confined and not lost. In an earlier analysis [6], we found a generally increasing, but saturating, trend of the fueling efficiency of individual pellets over the course of an injection sequence in W7-X. Additionally, a direct comparison showed, that LFS pellets are more successfully triggering FIT and hence fueling the core after some initial pellets have been injected: the peak probability in triggering the FIT was found for pellet number 5–10 for the LFS injection geometry, while HFS pellets did not need those initial pellets (cf first footnote of table 3). The effect of increasing fueling efficiencies throughout a pellet series was formerly explained by the so called 'pre-cooling' [5] which would also affect the penetration depth discussed in subsection 4.1. Beside the 'pre-cooling' mechanism, the evolution of the FIT-probability throughout a pellet series might be explained by the $\boldsymbol{E}_r \times \boldsymbol{B}$ - rotation discussed in section 3.2. We found hints of a correlation for the radial electric field $\boldsymbol{E}_r$ (up to $z = -2.9$ and $e = -0.27$; depending on the radial location) as well, but the analysis suffered from a poor data quality which resulted in rather high p values. A correlation to the size of the ion root electric field (negative sign of z and e indicating the advantage of an, in absolute terms, lager negative $\boldsymbol{E}_r$) would explain the difference between HFS and LFS pellets we found as well. LFS pellets benefit from the increasing speed of the $\boldsymbol{E}_r \times \boldsymbol{B}$ - rotation in the region where the plasmoids are formed ($s \approx 0.5$). The drift rotation shifts the LFS pellet material from locations of outward directed plasmoid $\boldsymbol{E}_{\nabla B} \times \boldsymbol{B}$ - drift to inward directed drift regions. Once the stronger ion root electric field established due to the early pellets of a sequence (cf

figure 7), the $\boldsymbol{E}_r \times \boldsymbol{B}$ - rotation is comparable to or up to ten times faster than the outward directed plasmoid $\boldsymbol{E}_{\nabla B} \times \boldsymbol{B}$ - drift with its velocity of $\sim\mathcal{O}(1 \times 10^3\,\mathrm{m\,s^{-1}}$ [2, 53, 54]). As a result, the difference in deposition depth between HFS and LFS pellets vanishes throughout the pellet series. For HFS pellets this mechanism does the exact opposite - shifting their material from favorable to unfavorable regions - which could be the explanation why they are slightly more successfully fueling the core in the early phase of the series in general. However the change in E_r saturates throughout the series as shown in figure 7 and so does the effect of the $\boldsymbol{E}_r \times \boldsymbol{B}$ - rotation. The overall disadvantageous dependency on higher pellet numbers ($z = -1.8$, $p = 8\%$, $e = -0.17$) could be an indicator for a growing negative feedback limiting the increase in plasma performance during long pellet series which we found earlier and published in [37] and [47]. It needs to be mentioned, that the number of a pellet as a parameter is not strictly linked to a certain density level. It rather combines density increase, pre-cooling and change in $\boldsymbol{E}_r$ for example and is not a physics quantity in a strict sense. It was used to understand and describe the general trend/behavior of the fueling / FIT throughout a pellet series.

4.3. Diamagnetic energy

The negative dependency ($z = -2.2$, $p = 3\%$, $e = -0.21$) on the global plasma energy content W_{dia} can be explained in the same manner (negative feedback). Anyhow, we still find more FIT cases in high performance plasmas/good confinement plasmas or better vice versa: core fueling (FIT-triggering) pellets lead to high performance plasmas, but after reaching high W_{dia}, the FIT-effect becomes less likely. It needs to be mentioned, that high performance so far was almost exclusively achieved with pellets & FIT effect at high (saturated) $\boldsymbol{E}_r$, which could generally flaw hypothesis testing for W_{dia}. However, core fueling did prove to be very relevant to reach high performance plasma scenarios, therefore it is important to better understand the negative feedback and to find ways to sustain core fueling/high performance plasma scenarios throughout and beyond pellet series or even transferring the underlying principles to other fueling sources.

4.4. Electron temperature, heating power and pellet injection frequency

As mentioned earlier, the so called 'pre-cooling' of the plasma by predecessor pellets increases the penetration and deposition depth of subsequent pellets [5] by lowering the plasma temperature and hence the ablation rate. While the ablation takes place mostly in the outer half of the plasma ($s > 0.5$) we found that lower electron temperatures T_e especially in the plasma core ($s \approx 0$) and at half radius ($s \approx 0.5$) act strongly beneficial on the FIT-effect (up to $z = -2.9$, $p = 0.4$, $e = -0.28$; depending on the radial location), which might further improve core fueling success by FIT on top of the pre-cooling effect. While a lower heating power P_{ECRH} ($z = -1.7$, $p = 10\%$, $e = -0.16$) lowering the core electron temperature might show a weak correlation, a higher pellet injection frequency f_{pellet} ($z = 1.1$, $p = 29\%$, $e = 0.10$) does not show a correlation. This supports the presumption, that the pre-cooling and FIT-effect to some extend are independent and are linked via the penetration depth only.

4.5. Ion temperature

Similar to T_e, low ion temperature T_i seem beneficial for the FIT-effect (up to $z = -4.8$, $p = 0.1$, $e = -0.46$; depending on the radial location). In fact T_i shows the strongest correlation among all analyzed parameters. It needs to be emphasized that one of the consequences of pellet injection itself is an increase in T_i due to stronger collisional coupling of the cooler ions and the hotter electrons [47]. Thus, a negative feedback throughout the pellets series as for W_{dia} seems natural. The strong T_i-dependency in the core and half-radius region is striking, as an effect size of $e \approx -0.5$ indicates. It can be concluded that this plasma region plays a central role for the FIT-effect.

4.6. Plasma β

It is that exact region, where the pellet induced density increase (located at $s \approx 0.5$) and temperature decrease (quickly reaching $s = 0$) transiently separate, before the FIT-effect might suck the pellet material from the deposition location into the core. Both n_e and T_e are essential factors of the plasma β. A future analysis should investigate, if the transient spacial separation of the n_e increase on one hand and the T_e decrease on the other hand is causal for the favorable dependency on low plasma pressure we found at $s \approx 0.5$ and $s \approx 0$ ($z = -3.0$, $p = 0.3$, $e = -0.29$ for $s \approx 0$).

4.7. HFS - LFS comparison

The FIT-effect seems less dependent on most of the analyzed parameters for the HFS pellets. This does not mean fewer HFS pellets trigger the FIT-effect in general. The opposite is the case: HFS pellets still have a much higher success rate compared to the LFS pellets. Therefore the dataset of HFS pellets not exhibiting the FIT-effect is rather small (ambiguous pellets were omitted). This might be an explanation, why statistical trends in the HFS pellet data are harder to find. For example, no significant dependency on β could be observed for HFS pellets alone, although the strong dependency found for LFS pellets was even increased combining both datasets.

Another peculiarity was, that only for HFS pellets we found a strong mass dependency of the FIT-effect. The reason might as well be found in the deposition phase, similar to the other relevant HFS-LFS-differences addressed in sections 4.1 and 4.2. With regard to the usually large difference in size between HFS and LFS pellets (factor of 2–3) and the favorable dependency only for HFS pellets, a plausible speculation would be, that a certain threshold in pellet size needs to be surpassed to trigger the FIT. From the penetration depth point-of-view this means, a certain size is obligatory for the pellet material to make it to the flux surfaces with beneficial transport conditions. This size might be usually overcome by the bigger LFS pellets, but not always by the smaller HFS pellets.

5. Discussion and conclusions

In this study the process of the injection of cryogenic hydrogen fueling pellets was analyzed with regards to the three different but partially overlapping transient phases: the ablation, deposition and fast transport of the pellet material occurring on timescales of one microsecond up to tens of milliseconds. A database of about 1000 individual pellets was employed for this purpose.

We found that the commonly accepted NGS model describes the ablation phase reasonable, but not precisely. As a consequence, it underestimates the penetration depth of the pellets injected to W7-X. A comparison to a heuristic parameterized model which was build on experimental data (IPAD) revealed a weaker T_e and a stronger n_e dependency. The Neutral Gas and Plasma Shielding model [55, 56] used by the HPI2 code is similar to the NGS model and could be benchmarked against these results in a future study. The IPAD-model fitted to the W7-X pellet data matches well and provides a starting point for theory improvements and pellet injection codes like HPI2 could include it for the time being. In a future step, adding information on the experimental T_e and n_e profile shapes could extend the model.

Furthermore, we gained a better understanding of the deposition process in stellarators like W7-X, which likewise needs to be adopted to the codes. Most importantly the poloidal $\boldsymbol{E}_r \times \boldsymbol{B}$ - drift rotation of the plasma in stellarators, which is not included in the standard pellet injection code HPI2, needs to be introduced. For the first time it was observed, that obviously the $\boldsymbol{E}_r \times \boldsymbol{B}$ - drift directly affects the pellet plasmoids, assumingly due to friction with the (mainly poloidally) rotating background plasma. This phenomenon is highly dynamic, as the plasmoids are simultaneously subjects to the parallel expansion along the magnetic field lines and the $\boldsymbol{E}_{\nabla B} \times \boldsymbol{B}$ - drift due to the electrostatic polarization inside the plasmoids. Currently the poloidal $\boldsymbol{E}_r \times \boldsymbol{B}$ - drift rotation is not considered in HPI2, because the code was developed for the axisymmetric tokamaks and later only adapted to the non-axisymmetric stellarators [42]. The main difference among the two machine designs is the direction of the $\boldsymbol{E}_r \times \boldsymbol{B}$ - drift rotation, dominated by the viscosity: the drift rotation is directed mainly in poloidal direction in a stellarator and more toroidal in a tokamak. The plasmoid material is carried away by an $\boldsymbol{E}_r \times \boldsymbol{B}$ - drift rotation in either device, but in a stellarator predominantly in poloidal direction, as indicated by the data shown above. In an axisymmetric tokamak this occurs mainly in toroidal direction, and hence, in direction of the parallel expansion of the plasmoid, which to the first order does not alter the plasmoid $\boldsymbol{E}_{\nabla B} \times \boldsymbol{B}$ - drift and consequently the deposition depth.

This explains why a large difference between HFS and LFS fueling efficiency as predicted by HPI2 was not found in W7-X. The poloidal $\boldsymbol{E}_r \times \boldsymbol{B}$ - drift rotation velocity in W7-X depends on the specific plasma conditions and was found to be of the same order up to one order larger than the plasmoid $\boldsymbol{E}_{\nabla B} \times \boldsymbol{B}$ - drift velocity. This means the material from LFS-injected pellets is quickly displaced to the HFS (and vice versa) even before the outward-directed plasmoid $\boldsymbol{E}_{\nabla B} \times \boldsymbol{B}$ - drift significantly reduces or increases the penetration of the LFS or HFS pellet material respectively. Thus in stellarators it seems acceptable to refrain from HFS fueling pellet injection in favor of the much simpler setup of LFS pellet injection, especially for fusion relevant design machines.

A strong $\boldsymbol{E}_r \times \boldsymbol{B}$ - drift rotation has been shown to contribute to equilibrated flux surfaces of elevated density ('ring' on the 2D tomograms). This appears to be related to the onset of a subsequent FIT event. Although it does not trigger the FIT on its own as shown in figure 8 case *III*), at least its radial position seems to have an influence on the FIT-effect.

The FIT-effect itself cannot be explained by neoclassical particle transport or diffusion. It might be linked to the turbulence-introduced pinch found in W7-X [57]. The experimental program 20180920.017 discussed in the referenced publication resembles typical pre-pellet-series plasma conditions. Nevertheless, the pellet injection introduces strong density and temperature perturbations, which most certainly affect the pinch as well.

The statistical analysis of the W7-X pellet database delivers some starting points to access the physics behind the FIT-effect. In addition to the radial electric field $\boldsymbol{E}_r$ discussed earlier, the dependencies on low T_i & T_e and the therewith associated (core) plasma β are most important, facilitating the effect especially for LFS-injected pellets.

Beside increasing the similarly important penetration dept via engineering optimization (e.g. higher pellet injection velocity), the understanding of the FIT-effect and its various consequences is a key endeavor to establish LFS pellet injection as an effective core fueling technique in future stellarator type machines. The discovery of the FIT-effect and that it occurs for both HFS and LFS pellets is very valuable for future fusion reactor operation scenarios. It appears from the results of our study, as though HFS injection may not be essential in a stellarator for core plasma fueling and subsequent high performance operation. It would make the design of a future reactor-type stellarator much less complex, i.e. because short and straight rather than long and bend injection tubes could be used or rather the injector itself could be situated on the outboard side of the torus. Based on these findings, it was decided for the future W7-X steady operation pellet injector to do without a HFS injection option. The new ITER-like injector is currently operating in its first experiment campaign. The 'blower-gun' type pellet injector was decommissioned in return.

Acknowledgments

The author would like to thank F. Warmer for our fruitful discussions. This work has been carried out within the framework of the EUROfusion Consortium, funded by the European Union via the Euratom Research and Training Programme (Grant Agreement No. 101052200—EUROfusion). Views and opinions expressed are however those of the author(s) only and do not necessarily reflect those of the European Union or the European Commission. Neither the European Union nor the European Commission can be held responsible for them.

Note added. The data analysis and processing codes used for this paper can be found in https://git.ipp-hgw.mpg.de/hdamm/papers/-/tree/fbe762a03da0125b8656d846375e582e15268aed/Pellet_Deposition, https://git.ipp-hgw.mpg.de/hdamm/data_eval/-/tree/dcad81e06cd214dbce6a547f182b6aadadbce4a7 and https://git.ipp-hgw.mpg.de/hdamm/ts_archive_2_profiles/-/tree/7bd4bb0b6d0696a76c761d9779d636fc789b0337.

Appendix. Statistical method

To identify cases of successfully core fueling pellet injections and markers thereof, the Mann–Whitney U hypothesis test [58] was employed. It is a statistical method to test the probability of a randomly selected sample x from distribution X being larger or smaller than a randomly selected sample y from distribution Y. In this study, the test was performed on two distributions, where c_i denotes the i^{th} sample from the distribution C of successfully core-fueling injections and e_j denotes the j^{th} sample from the distribution E of edge fueling (or failed core-fueling) samples for the different parameters from the W7-X pellet injection database. In each individual test case C and E are distributed along the respectively analyzed parameter. The aim of the test was to examine, whether or not the fast rise in central electron density after the injection of a pellet was correlated to the analyzed parameter - in other words: whether the null hypothesis 'The core-fueling success was independent from the analyzed parameter.' could be rejected.

The Mann–Whitney U test statistic reads:

$$U = \sum_{i=1}^{n_c} \sum_{j=1}^{n_e} \mathrm{S}\left(c_i, e_j\right), \tag{A.1}$$

where $\mathrm{S}(c_i, e_j) = 1$ for $c_i > e_j$, $\mathrm{S}(c_i, e_j) = 1/2$ for $c_i = e_j$ ('tie') and $\mathrm{S}(c_i, e_j) = 0$ for $c_i < e_j$.

The Mann–Whitney U test rejects the null hypothesis for too large or too small U. For large samples a computational approach employing numeric ranking to implement the comparison of all samples can be derived as:

$$U_{\mathrm{c/e}} = \mathrm{R}_{\mathrm{c/e}} - \frac{n_{\mathrm{c/e}}\left(n_{\mathrm{c/e}} + 1\right)}{2}, \tag{A.2}$$

where $n_{\mathrm{c/e}}$ is the sample size and $\mathrm{R}_{\mathrm{c/e}}$ is the sum of adjusted ranks in distributions C or E respectively.

For large samples, U is approximately normally distributed [59] and a standard score (z-score) can be formulated as:

$$z = \frac{U_{\mathrm{c/e}} - m_U}{\sigma_U}, \tag{A.3}$$

where $m_U = (n_c \cdot n_e)/2$ is the mean [60] and

$$\sigma_U = \sqrt{\frac{n_c n_e}{12}\left((n+1) - \frac{\sum_{k=1}^{K}\left(t_k^3 - t_k\right)}{n\left(n-1\right)}\right)}, \tag{A.4}$$

with $n = n_c + n_e$, t_k = number of ties of the k^{th} rank and K = total number of tied ranks [61] is the standard deviation.

The 'z-Score' represents the number of standard deviations by which the obtained statistic is different from the statistic expected, if the null hypothesis would hold. Similarly the 'p-Value' can be employed to quantify the significance of a test result. It delivers the probability of obtaining test results at least as extreme as given by the data, if the null hypothesis holds.

The p-Value, σ_U and m_U are not independent from one another:

$$m_U = n \cdot p, \tag{A.5}$$

$$\sigma_U = \sqrt{\left(p\left(1-p\right)/n\right)}. \tag{A.6}$$

Commonly, $|z| > 2\sigma$ and $p < 5\%$ are selected as sufficient significance levels to reject the null hypothesis.

If the test was successful (e.g. the null hypothesis could be rejected), the 'effect size':

$$e = \frac{z}{\sqrt{n_c + n_e}} \tag{A.7}$$

can be employed as a measure for the strength of the relation between the feature and the test variable. It ranges from 0 to 1. Typically, an effect size $e < 0.1$ indicates a weak effect whereas effect sizes $e > 0.5$ indicate strong effects. The sign of e denotes a positive $(+)$ or negative $(-)$ dependency in the analyzed range of the variable.

The Mann–Whitney U test was selected because the distributions are not necessarily interval scaled, in which case the more commonly used t-Test would fail [62]. In contrast to the Fligner–Policello test [63], the Mann–Whitney U test is also not simply a test of equal means, e.g. even if the medians are numerically equal, it is possible that the Mann–Whitney U test rejects the null hypothesis, if the shape and dispersion of the two populations differ. The Brunner–Munzel test would be an appropriate alternative to the Mann–Whitney U test, if certain conditions would not be satisfied by the two distributions C and E, i.e. if their variances differ significantly [64, 65]. Nevertheless, the Mann–Whitney U test shows a small power advantage over Brunner–Munzel for skewed data with unequal sample size [66] which could be found in our database. We compared the results for the p-Value of the Brunner–Munzel test and the Mann–Whitney U test, finding they delivered virtually identical outcomes. Therefore only the Mann–Whitney U test results are presented in this work.

ORCID iDs

H. Damm 0000-0001-9423-1608
R.C. Wolf 0000-0002-2606-5289
J. Schilling 0000-0002-6363-6554
N. Panadero 0000-0003-0462-2432
S.A. Bozhenkov 0000-0003-4289-3532
C. Brandt 0000-0002-5455-4629
K.J. Brunner 0000-0002-0974-0457

G. Fuchert 0000-0002-6640-2139
S. Kwak 0000-0001-7874-7575

References

[1] Pegourie B. 2007 Review: pellet injection experiments and modelling *Plasma Phys. Control. Fusion* **49** R87
[2] Knoop M., Madsen N. and Thompson R.C. 2016 *Trapped Charged Particles—A Graduate Textbook With Problems and Solutions* (World Scientific)
[3] Baylor L.R. *et al* 1992 Pellet fuelling deposition measurements on JET and TFTR *Nucl. Fusion* **32** 2177
[4] Lang P.T., Büchl K., Kaufmann M., Lang R.S., Mertens V., Müller H.W. and Neuhauser J. (ASDEX Upgrade) 1997 High-efficiency plasma refuelling by pellet injection from the magnetic high-field side into ASDEX Upgrade *Phys. Rev. Lett.* **79** 1487–90
[5] Baldzuhn J. *et al* (Wendelstein 7-X Team) 2018 Particle fueling experiments with a series of pellets in LHD *Plasma Phys. Control. Fusion* **60** 035006
[6] Baldzuhn J. *et al* 2019 Pellet fueling experiments in Wendelstein 7-X *Plasma Phys. Controled Fusion* **61** 095012
[7] Parks P., Turnbull R. and Foster C. 1977 A model for the ablation rate of a solid hydrogen pellet in a plasma *Nucl. Fusion* **17** 539
[8] Kaufmann M., Lackner K., Lengyel L. and Schneider W. 1986 Plasma shielding of hydrogen pellets *Nucl. Fusion* **26** 171
[9] Spitzer jr. L. 1958 The stellarator concept *Phys. Fluids* **1** 253–64
[10] Sakharov A.D. 1959 *Theory of Magnetic Thermonuclear Reactors [in Russian: Fizika Plazmy i Problema Upravliaemykh Termoiadernikh Reaktsii]* vol 1 (Pergamon) (available at: https://books.google.de/books?id = V8zvAAAAMAAJ) pp 20–30
[11] Tamm I.E. 1959 *Theory of Magnetic Thermonuclear Reactors [in Russian: Fizika Plazmy i Problema Upravliaemykh Termoiadernikh Reaktsii]* vol 1 (Pergamon) (available at: https://books.google.de/books?id = V8zvAAAAMAAJ) pp 3–19
[12] Rozhansky V., Veselova I. and Voskoboynikov S. 1995 Evolution and stratification of a plasma cloud surrounding a pellet *Plasma Phys. Control. Fusion* **37** 399
[13] Hastings D., Houlberg W. and Shaing K. 1985 The ambipolar electric field in stellarators *Nucl. Fusion* **25** 445
[14] Helander P. 2007 On rapid plasma rotation *Phys. Plasmas* **14** 104501
[15] Turkin Y., Beidler C.D., Maaßberg H., Murakami S., Tribaldos V. and Wakasa A. 2011 Neoclassical transport simulations for stellarators *Phys. Plasmas* **18** 022505
[16] Langenberg A. *et al* (Wendelstein 7-X Team) 2018 Prospects of x-ray imaging spectrometers for impurity transport: recent results from the stellarator Wendelstein 7-X (invited) *Rev. Sci. Instrum.* **89** 10G101
[17] Baldzuhn J., Kick M. and Maassberg H. (the W7-AS Team) 1998 Measurement and calculation of the radial electric field in the stellarator W7-AS *Plasma Phys. Control. Fusion* **40** 967
[18] Beidler C. *et al* 1990 Physics and engineering design for Wendelstein 7-X *Fusion Technol.* **17** 148–68
[19] Damm H. *et al* (the Wendelstein 7-X Team) 2019 First results from an event synchronized—high repetition Thomson scattering system at Wendelstein 7-X *J. Instrum.* **14** C09037
[20] Ingesson L.C., Alper B., Peterson B.J. and Vallet J.-C. 2008 Chapter 7: tomography diagnostics: bolometry and soft-x-ray detection *Fusion Sci. Technol.* **53** 528–76
[21] Pasch E., Beurskens M.N.A., Bozhenkov S.A., Fuchert G., Knauer J. and Wolf R.C. 2016 The Thomson scattering system at Wendelstein 7-X *Rev. Sci. Instrum.* **87** 11E729
[22] Brandt C. *et al* (the W7-X Team) 2020 Soft x-ray tomography measurements in the Wendelstein 7-X stellarator *Plasma Phys. Control. Fusion* **62** 035010
[23] Bosch H.-S. *et al* (W7-X Team) 2017 Final integration, commissioning and start of the Wendelstein 7-X stellarator operation *Nucl. Fusion* **57** 116015
[24] Dibon M. *et al* 2015 Blower gun pellet injection system for W7-X *Fusion Eng. Des.* **98–99** 1759–62
[25] Gruber O., Kaufmann M., Köppendörfer W., Lackner K. and Neuhauser J. 1984 Physics background of the ASDEX Upgrade project *J. Nucl. Mater.* **121** 407–14
[26] Bozhenkov S.A. *et al* 2017 The Thomson scattering diagnostic at Wendelstein 7-X and its performance in the first operation phase *J. Instrum.* **12** 10004
[27] Knauer J., Korneje P., Mora H.T., Hirsch M., Werner A. and Wolf R.C. 2016 A new dispersion interferometer for the stellarator Wendelstein 7-X *43rd EPS Conf. on Plasma Physics, European Physical Society. Leuven, Belgium* ed P. Mantica p 4.017
[28] Svensson J. (JET EFDA contributors) 2011 Non-parametric tomography using gaussian processes *JET-EFDA Internal Report EFDA–JET–PR(11)24* (available at: https://scipub.euro-fusion.org/wp-content/uploads/eurofusion/EFDP11024.pdf)
[29] Schilling J., Thomsen H., Brandt C., Kwak S. and Svensson J. (W7-X Team) 2021 Soft x-ray tomograms are consistent with the magneto-hydrodynamic equilibrium in the Wendelstein 7-X stellarator *Plasma Phys. Control. Fusion* **63** 055010
[30] Wesson J. and Campbell D. 2004 *Tokamaks* (Oxford University Press) (available at: https://edisciplinas.usp.br/pluginfile.php/5914191/course/section/6090251/Tokamaks_Wesson.pdf)
[31] Bozhenkov S., Geiger J., Grahl M., Kißlinger J., Werner A. and Wolf R. 2013 Service oriented architecture for scientific analysis at W7-X an example of a field line tracer *Fusion Eng. Des.* **88** 2997–3006
[32] Hirshman S., van RIJ W. and Merkel P. 1986 Three-dimensional free boundary calculations using a spectral Green's function method *Comput. Phys. Commun.* **43** 143–55
[33] Langenberg A., Svensson J., Thomsen H., Marchuk O., Pablant N., Burhenn R. and Wolf R. 2016 Forward modeling of x-ray imaging crystal spectrometers within the Minerva Bayesian analysis framework *Fusion Sci. Technol.* **69** 560–7
[34] Rahbarnia K. *et al* (W7-X Team) 2018 Diamagnetic energy measurement during the first operational phase at the Wendelstein 7-X stellarator *Nucl. Fusion* **58** 096010
[35] Velasco J. *et al* (the TJ-II Team) 2016 Particle transport after pellet injection in the TJ-II stellarator *Plasma Phys. Control. Fusion* **58** 084004
[36] Dinklage A. *et al* the LHD Experiment Group 2017 The effect of transient density profile shaping on transport in large stellarators and heliotrons *Nucl. Fusion* **57** 066016
[37] Baldzuhn J. *et al* (W7-X Team) 2020 Enhanced energy confinement after series of pellets in Wendelstein 7-X *Plasma Phys. Control. Fusion* **62** 055012
[38] Parks P. and Turnbull R. 2024 Effect of transonic flow in the ablation cloud on the lifetime of a solid hydrogen pellet in a plasma *Phys. Fluids* **21** 1735–41
[39] Baylor L. *et al* 1997 An international pellet ablation database *Nucl. Fusion* **37** 445
[40] Moré J.J. 1978 *The Levenberg-Marquardt Algorithm: Implementation and Theory* ed G.A. Watson (Springer)
[41] Pegourie B., Waller V., Dumont R.J., Eriksson L.-G., Garzotti L., Géraud A. and Imbeaux F. 2004 Modelling of pellet ablation in additionally heated plasmas *Plasma Phys. Control. Fusion* **47** 17

[42] Koechl F. et al Modelling of pellet particle ablation and deposition: the hydrogen pellet injection code HPI2 *Preprint EFDA–JET–PR(12)57* (available at: https://scipub.euro-fusion.org/wp-content/uploads/2014/11/EFDP12057.pdf)
[43] Panadero N. 2018 A study of the physics of pellet injection in magnetically confined plasma in stellarators *PhD Thesis* Centre for Energy Environmental and Technological Research (CIEMAT) (available at: https://info.fusion.ciemat.es/PhDThesis/Panadero.pdf)
[44] Erckmann V. *et al* (W7-X ECRH Team at IPP Greifswald, W7-X ECRH Team at FZK Karlsruhe & W7-X ECRH Team at IPF Stuttgart) 2007 Electron cyclotron heating for W7-X: physics and technology *Fusion Sci. Technol.* **52** 291–312
[45] Pablant N.A. *et al* (W7-X Team) 2018 Core radial electric field and transport in Wendelstein 7-X plasmas *Phys. Plasmas* **25** 022508
[46] Helander P. *et al* 2012 Stellarator and tokamak plasmas: a comparison *Plasma Phys. Control. Fusion* **54** 124009
[47] Bozhenkov S. *et al* (W7-X Team) 2020 High-performance plasmas after pellet injections in Wendelstein 7-X *Nucl. Fusion* **60** 066011
[48] Rice J., Citrin J., Cao N., Diamond P., Greenwald M. and Grierson B. 2020 Understanding LOC/SOC phenomenology in tokamaks *Nucl. Fusion* **60** 105001
[49] Rahbarnia K. *et al* (Wendelstein 7-X Team) 2020 Alfvénic fluctuations measured by in-vessel mirnov coils at the Wendelstein 7-X stellarator *Plasma Phys. Control. Fusion* **63** 015005
[50] Mendes S.V. *et al* (the W7-X Team) 2023 Broadband alfvénic excitation correlated to turbulence level in the Wendelstein 7-X stellarator plasmas *Nucl. Fusion* **63** 096008
[51] Riemann J. *et al* 2025 Excitation of Alfvénic modes via electromagnetic turbulence in Wendelstein 7-X *Phys. Rev. Lett.* **134** 025103
[52] Krämer-Flecken A. *et al* (W7-X Team) 2025 Observation and characterisation of trapped electron modes in Wendelstein 7-X *Plasma Phys. Control. Fusion* **67** 025014
[53] Matsuyama A., Koechl F., Pégourié B., Sakamoto R., Motojima G. and Yamada H. 2012 Modelling of the pellet deposition profile and B-induced drift displacement in non-axisymmetric configurations *Nucl. Fusion* **52** 123017
[54] Panadero N. *et al* (TJ-II Team and W7-X Team) 2018 Experimental studies and simulations of hydrogen pellet ablation in the stellarator TJ-II *Nucl. Fusion* **58** 026025
[55] Houlberg W., Milora S. and Attenberger S. 1988 Neutral and plasma shielding model for pellet ablation *Nucl. Fusion* **28** 595
[56] Pegourie B., Picchiottino J.-M., Drawin H.-W., Geraud A. and Chatelier M. 1993 Pellet ablation studies on Tore Supra *Nucl. Fusion* **33** 591
[57] Thienpondt H. *et al* 2023 Prevention of core particle depletion in stellarators by turbulence *Phys. Rev. Res.* **5** L022053
[58] Mann H. and Whitney D. 1947 On a test of whether one of two random variables is stochastically larger than the other *Ann. Math. Stat.* **18** 50–60
[59] Eckstein P.P., Rönz B., Strohe H.G., Götze W. and Hartl F. 1994 *Lexikon Statistik* 1st edn (Gabler Verlag)
[60] Siegel S. 1956 *Nonparametric Statistics for the Behavioral Sciences* (McGraw-Hill)
[61] Lehmann E. and D'Abrera H. 1998 *Nonparametrics: Statistical Methods Based on Ranks* (Prentice Hall) (available at: https://books.google.de/books?id = zNNFAQAAIAAJ)
[62] Fay M. and Proschan M. 2010 Wilcoxon-Mann-Whitney or t-test? On assumptions for hypothesis tests and multiple interpretations of decision rules *Stat. Surv.* **4** 1–39
[63] Fong Y. and Huang Y. 2019 Modified Wilcoxon–Mann–Whitney test and power against strong null *Am. Stat.* **73** 43–49
[64] Pratt J.W. 1964 Risk aversion in the small and in the large *Econometrica* **32** 122–36
[65] Divine G.W., Norton H.J., Barón A.E. and Juarez-Colunga E. 2018 The Wilcoxon–Mann–Whitney procedure fails as a test of medians *Am. Stat.* **72** 278–86
[66] Karch J.D. 2021 Psychologists should use Brunner-Munzel's instead of Mann-Whitney's *U* test as the default nonparametric procedure *Adv. Methods Pract. Psychol. Sci.* **4**